Identification of image artifacts from internal multiples

Alison E. Malcolm[1], Maarten V. de Hoop[2], and Henri Calandra[3]

ABSTRACT

First-order internal multiples are a source of coherent noise in seismic images because they do not satisfy the single-scattering assumption fundamental to most seismic processing. There are a number of techniques to estimate internal multiples in data; in many cases, these algorithms leave some residual multiple energy in the data. This energy produces artifacts in the image, and the location of these artifacts is unknown because the multiples were estimated in the data before the image was formed. To avoid this problem, we propose a method by which the artifacts caused by internal multiples are estimated directly in the image. We use ideas from the generalized Bremmer series and the Lippmann-Schwinger scattering series to create a forward-scattering series to model multiples and an inverse-scattering series to describe the impact these multiples have on the common-image gather and the image. We present an algorithm that implements the third term of this series, responsible for the formation of first-order internal multiples. The algorithm works as part of a wave-equation migration; the multiple estimation is made at each depth using a technique related to one used to estimate surface-related multiples. This method requires knowledge of the velocity model to the depth of the shallowest reflector involved in the generation of the multiple of interest. This information allows us to estimate internal multiples without assumptions inherent to other methods. In particular, we account for the formation of caustics. Results of the techniques on synthetic data illustrate the kinematic accuracy of predicted multiples, and results on field data illustrate the potential of estimating artifacts caused by internal multiples in the image rather than in the data.

INTRODUCTION

That internal multiples are present in seismic experiments has been acknowledged for a long time (Sloat, 1948). At present, significantly more is known about attenuation of surface-related multiples (Anstey and Newman, 1966; Kennett, 1974; Aminzadeh and Mendel, 1980; Fokkema and van den Berg, 1993; Berkhout and Verschuur, 1997; Verschuur and Berkhout, 1997; Weglein et al., 1997, 2003) than is known about attenuation of internal multiples (Fokkema et al., 1994; Weglein et al., 1997; Jakubowicz, 1998; Kelamis et al., 2002; ten Kroode, 2002; van Borselen, 2002; Weglein et al., 2003; Berkhout and Verschuur, 2005; Verschuur and Berkhout, 2005). With the exception of techniques such as the angle-domain filtering proposed by Sava and Guitton (2005) and the image-domain surface-related multiple prediction technique of Artman and Matson (2006), the current state of the art in multiple attenuation involves estimating multiples in the data. We propose an algorithm for estimating imaging artifacts caused by internal multiples directly on image gathers and images, as part of a wave-equation imaging procedure of the downward continuation type.

Fokkema and van den Berg (1993) used reciprocity, along with the representation theorem, to show that it is possible to predict surface-related multiples from seismic reflection data and that this prediction can be carried out through a Neumann series expansion. This idea is fundamental to surface-related (SRME) and internal multiple estimation techniques of Berkhout and Verschuur (Berkhout and Verschuur, 1997, 2005; Verschuur and Berkhout, 1997, 2005); other authors have also built upon these ideas (Fokkema et al., 1994; Kelamis et al., 2002; van Borselen, 2002). The technique discussed here has its roots in these ideas but differs from other methods because we propose estimating, directly in the image, artifacts caused by internal multiples (IM). This approach is in contrast to previous methods that estimate IM and subtract them from the data before an image is formed. We develop and test our method specifically for first- or leading-order internal multiples, but the extension to higher orders is

straightforward. The series used to estimate image artifacts caused by IM is a hybrid between the Lippmann-Schwinger scattering series used by Weglein et al. (1997) and the generalized Bremmer coupling series, a Neumann series, introduced by de Hoop (1996).

The Lippmann-Schwinger series was introduced by Lippmann (1956) to model particle scattering. In the development of this series, the problem is first solved in a known background model, giving an incorrect solution. A series is then developed to better approximate the correct solution, with terms in the series being of successively higher order in a contrast operator. (The contrast operator is the difference between the operator in the known background model and the same operator in the true model.) This idea was developed further by Moses (1956) and Prosser (1969) for the quantum scattering problem and by Razavy (1975) for the wave equation. Weglein et al. (1997) use this series for the exploration seismic problem to develop techniques for surface and internal-multiple attenuation; they choose water velocity as the known reference model. Ten Kroode (2002) gives a detailed asymptotic description of a closely related approach to attenuate internal multiples and notes that his method correctly estimates internal multiples when two (sufficient) assumptions are satisfied. The first assumption is that there are no caustics in the wavefield, and the second is the so-called total traveltime monotonicity condition. This condition is illustrated in Figure 1 and shows that a wave excited at s and scattered at depth z_1 will arrive at the surface in less time than a wave following the same path from s to z_1, but continuing on to scatter at the deeper depth z_2. Nita and Weglein (personal communication) show that the total traveltime monotonicity assumption is not necessary for the method proposed by Weglein et al. (1997) and discuss further the assumptions behind this method.

The Bremmer series was introduced for planarly layered (1D) models by Bremmer (1951). The convergence of this series is discussed by Atkinson (1960) and Gray (1983). An extension to 2D configurations is given by Corones (1975); the convergence of this extension is discussed by McMaken (1986). De Hoop (1996) generalizes this series to laterally heterogeneous models in higher dimensions and shows that this generalization is convergent. In the Bremmer series, the wavefield is split into up- and downgoing constituents; these constituents are then coupled through reflection and transmission operators. Each term involves one more reflection/transmission and propagation step than the previous term. The first term of the series models direct waves, the second models singly scattered waves (where scattering may be reflection or transmission), and so on. This series has been applied in many problems (see
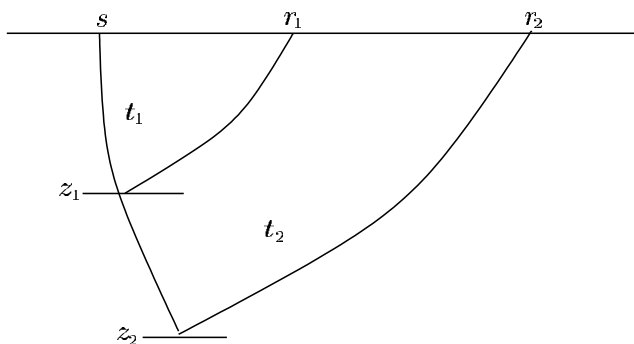

Figure 1. Illustration of the traveltime monotonicity assumption. The assumption states that if $z_1 < z_2$, then $t_1 < t_2$, provided the two scattering points lie on the same path.

van Stralen, 1997, for an overview). Aminzadeh and Mendel (1980, 1981) were the first to propose a method using the Bremmer series to attenuate surface-related multiples in a horizontally layered medium. More recently, a method proposed by Jakubowicz (1998) uses implicitly a form of the generalized Bremmer series. Although the generalized Bremmer series can be extended to account for turning-ray waves, we keep the standard assumption that rays are nowhere horizontal.

We use the generalized Bremmer coupling series to model internal multiples because its behavior and convergence are known (de Hoop, 1996). We replace reflection and transmission operators in this series, which depend on the full velocity model, with contrast operators that distinguish the smooth background-velocity model from the reflectors. This approach leads to the construction of a hybrid series, using the contrast-source formulation from the Lippmann-Schwinger scattering equation (Lippmann, 1956; Weglein et al., 1997). By constructing jointly a forward (modeling) series and an inverse (imaging) series and combining them, we can estimate artifacts caused by IM directly in the image. The method requires knowledge of the velocity model to form the image; however, errors in this model deeper than the depth of the shallowest reflector involved in the generation of internal multiples (the depth of the up-to-down reflection) do not influence the estimation of the artifacts. We do not require the traveltime monotonicity assumption (ten Kroode, 2002) and admit the formation of caustics. The construction of the hybrid series is discussed in Malcolm and de Hoop (2005); a summary is given in the appendices to this paper.

We discuss an algorithm to implement the third term of this hybrid series that combines ideas from wave-equation migration and SRME. Our technique is related to the technique recently developed by Artman and Matson (2006) that predicts surface-related multiples as part of a shot-record migration algorithm. Here, common-midpoint wave-equation migration techniques are used to downward continue the recorded data into the subsurface, where an estimate of the multiples generated at each depth is made. These estimated multiples are then added to a second data wavefield, from which an estimate of image artifacts is formed. The work of Artman and Matson avoids propagation of this second wavefield, requiring only a second imaging condition. Their technique requires shot-record migration, however, and is currently limited to the surface-related multiples case.

PROCEDURE TO ESTIMATE ARTIFACTS

Multiples cause artifacts in images because they do not satisfy the single-scattering assumption. We propose a method for estimating these artifacts that can be performed as part of a downward-continuation migration as formulated by Stolk and de Hoop (2006). We give some details on how the theory of the method is developed in Appendices A and B. We describe here the algorithm used to estimate artifacts caused by multiples, following the flowchart shown in Figure 2.

In the first step of this procedure, labeled (a) in Figure 2, the data d recorded at the surface are downward continued to depth z, yielding $\tilde{d}(z)$. This step is part of standard downward-continuation or survey-sinking migration (Claerbout, 1970, 1985), using the double square-root (DSR) equation. The depth z is not necessarily the depth of a multiple-generating layer. It is because we use the data downward continued to z to estimate the multiples that we do not require the traveltime monotonicity assumption of ten Kroode (2002); caustics

are dealt with naturally in downward-continuation migration.

The algorithm used to estimate the data at depth z from the data at the surface is not of particular importance. The propagator used to generate examples shown here falls into the category of a generalized screen propagator. It is implemented as a split-step propagator along with an implicit finite-difference residual wide-angle correction. This particular algorithm was proposed by Jin et al. (1998). By using this algorithm, we expect to have kinematically accurate estimates of the artifacts from internal multiples. Theoretically, the amplitudes are also dealt with accurately within the framework presented for single scattering by Stolk and de Hoop (2005, 2006) along with extension to multiples given in Malcolm and de Hoop (2005). A discussion of the implementation of these amplitude factors is beyond the scope of this work.

In the next step of the algorithm, (b) in Figure 2, the multiples $\tilde{d}_3$, also downward continued to depth z, are estimated by

$$\tilde{d}_3(z,s,r,t) \approx -\partial_t^2 \int \int Q^*_{-,s'}(z)(E_1 a_1)(z,s',r')$$
$$\times Q^*_{-,r'}(z)\tilde{d}(z,s',r,\ \cdot\ )^{(t)} * \tilde{d}(z,s,r',\ \cdot\ )ds'dr'. \tag{1}$$

In this paper we implement an approximation to this equation, leaving out the Q factors.

Equation 1 describes a procedure that is divided into three parts. The first step is to convolve the two downward-continued $\tilde{d}$ data sets. This step is reminiscent of the SRME procedure of Fokkema and van den Berg (1993), Berkhout and Verschuur (1997), and as well as the works of Weglein et al. (1997). This step estimates multiples that could be generated at the depth z. The second step, labeled (d) in Figure 2, involves synthesizing a true-amplitude image, a_1, from the downward-continued data $\tilde{d}$. For the description given here, the imaging operator in Stolk and de Hoop (2006, equation 2.26) should be applied. This imaging operator correctly accounts for the Q operators and contains the standard $h = 0$ and $t = 0$ imaging condition. This step gives an estimate a_1 of a; it is only an estimate because it uses all of the data, whereas the true image a uses only the primaries. It is here that we make an approximation in the numerical examples, by using only the standard $t = 0$ and $h = 0$ imaging condition and not accounting for the Q operators. The third step, labeled (e) in Figure 2, is the multiplication of the convolved data by this estimate a_1 at the $s' = r'$ point (see Figure 3 for a diagram of the location of these points). The $E_1:a_1(z,x) \to \delta(s'-r')a_1\left(z,\frac{s'+r'}{2}\right)$ operator is an extension from image to data coordinates, used to transform a_1, which is a function of the spatial position $(z,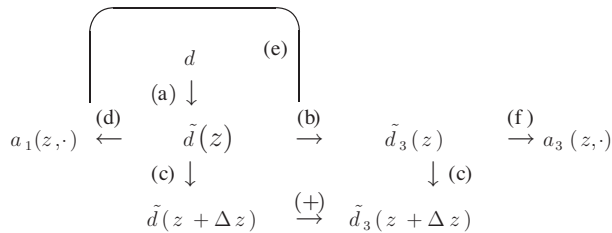x)$ into a function dependent on the source and receiver positions s' and r'. Multiplying by a_1 implicitly ensures that only the multiples that would be truly generated at this depth are included in the estimation. To remove the approximation in equation 1, primaries-only data $\tilde{d}_1$ would have to be substituted for the $\tilde{d}$ and a primaries-only image a would have to be used in place of a_1. These replacements are justified in Appendix B.

Although, in the examples, we do not make true-amplitude images, for either the all-data image or the estimated artifacts, it is worth noting that the only amplitude factors missing in the estimation of the multiples in equation 1 are the operators $Q^*_{-,s'}$ and $Q^*_{-,r'}$. The Q operators decompose the wavefield into its up- and downgoing constituents, a necessary step in the development of downward-continuation migration detailed in Stolk and de Hoop (2005, equation 1.8). The minus subscript indicates that these operators are responsible for extracting the downgoing rather than upgoing constituents, the subscripts s' or r' determine whether the operator is applied in source or receiver coordinates, and the * indicates that these operators in fact recompose the wavefield into the total wavefield rather than decomposing. Including both these Q^* operators and using a true-amplitude image for a_1 are necessary to obtain consistent amplitudes between the estimated artifacts and the artifacts in the image. Omitting these operators can result in a large difference in absolute amplitude between the image and estimated artifacts. As shown in the numerical examples given in this paper, the influence on the shape of the estimated multiples is much smaller, as is discussed further in Appendix A.

When data are downward continued from the surface to depth z, energy from depths shallower than z will remain in the downward-continued data, appearing at negative times. This effect is not a problem for imaging because typical imaging procedures use the downward-continued data only at time $t = 0$. Our technique of estimating multiples uses all of the downward-continued data, however. For equation 1 to be valid, negative times must be removed from the downward-continued data. When the reflectors are separated by enough time, the negative times can be removed with a simple time-windowing procedure. In some situations, we find a τ-p filter to be more effective because there are typically tails at small positive and negative times caused by the band-limitation/restricted illumination of the data.
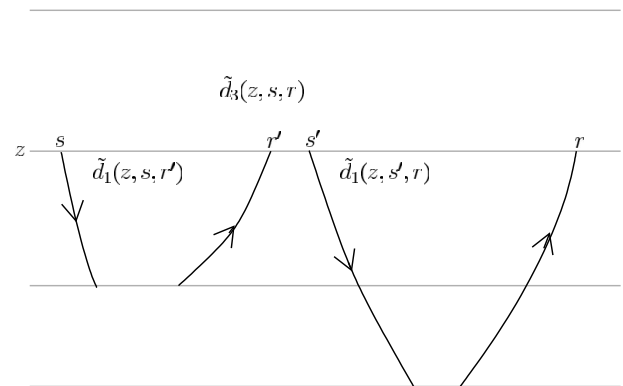

Figure 3. Illustration of equation 1, the estimation of the multiple at depth z. The lines represent wavepaths rather than rays and do not connect because the imaging condition has not been applied. In the algorithm, the downward-continued, singly scattered data $\tilde{d}_1$ are estimated with the downward-continued data, $\tilde{d}$.

Figure 2. Flowchart illustrating the algorithm used to estimate artifacts directly in the image.

To compare the artifacts in the image with estimated artifacts, an image must also be formed with the estimated multiples; this is (f) in Figure 2. This image, denoted a_3, is formed in the manner discussed in (b) of Figure 2. It is interesting to note that the agreement between the image artifacts and the estimated artifacts does not depend on the choice of velocity model below the depth of the up-to-down reflection (z in Figure 3) because the true and estimated multiples will see the same error.

This procedure completes one depth step of the algorithm. After the above tasks are complete, both the wavefield and the estimate multiples are downward continued to the next depth level, $z + \Delta z$, which is step (c) in Figure 2. At this depth step, the entire procedure is repeated with the multiples estimated at this new depth added to the downward-continued multiples from the previous depth.

In equation 1, two data sets, each containing a source wavelet, are convolved together to estimate the multiples. As in other techniques in which multiples are estimated through such a convolution, an accurate estimate requires that one copy of this wavelet be deconvolved from the estimated multiples. In addition, as the data are downward continued into the subsurface, the range of data offsets containing significant energy will become narrower. That narrow offsets will be available is advantageous for multiple prediction, but

the lack of larger offsets may be detrimental in some situations. Further, to obtain accurate amplitude estimates, corrections should be made for differences in illumination between multiples and primaries.

EXAMPLES

In this section, we describe the results of applying the technique to data. Three different synthetic models are presented. A flat-layered model illustrates the steps of the algorithm. Following this description, a more complicated model is used to test the ability of the method to estimate imaging artifacts caused by IM in the presence of caustics and to test the sensitivity of the method to the velocity model. We also present a field-data example, consisting of a 2D line extracted from a 3D survey in the Gulf of Mexico.

The displayed images, for both a_1 and a_3, have had automatic gain control (AGC) applied to enhance the multiple contribution. Computational artifacts such as Fourier wrap-around and computational boundary effects were suppressed, but not fully eliminated, in the downward continuation by padding with zeros and tapering the data in both midpoint and offset. In most figures, the true reflectors are clipped to show artifacts more clearly. Although the wavelet has not been deconvolved, the data have been shifted in time so that the peak of the source wavelet is at zero time and bandpass filtered to match the frequency content of the two images. The synthetic examples in Figures 4–11 are shown with an aspect ratio of 1/4.

Flat model

The model in the first example consists of a single layer, extending from 1.5 to 2.5 km, with a velocity of 2 km/s; the layer is embedded in a homogeneous model with velocity 6 km/s. Synthetic data were computed in this model with finite-difference modeling; 101 midpoints were generated with 101 offsets at each midpoint and a spacing of 15 m in both midpoint and offset (we define offset as $(r - s)/2$); 4 s of data were computed at 4-ms sampling, with a peak frequency of 10 Hz and a maximum frequency of 20 Hz. To image these data, a depth step of 10 m was used.

In our method, the data are first downward continued as part of a standard wave-equation migration technique, i.e., (a) in Figure 2. In Figure 4a, we show $\tilde{d}(z = 1.5 \text{ km})$, a downward-continued CMP gather at the depth $z = 1.5$ km from the top of the layer. The primary reflected from the top of the layer is located around $t = 0$, the reflec-
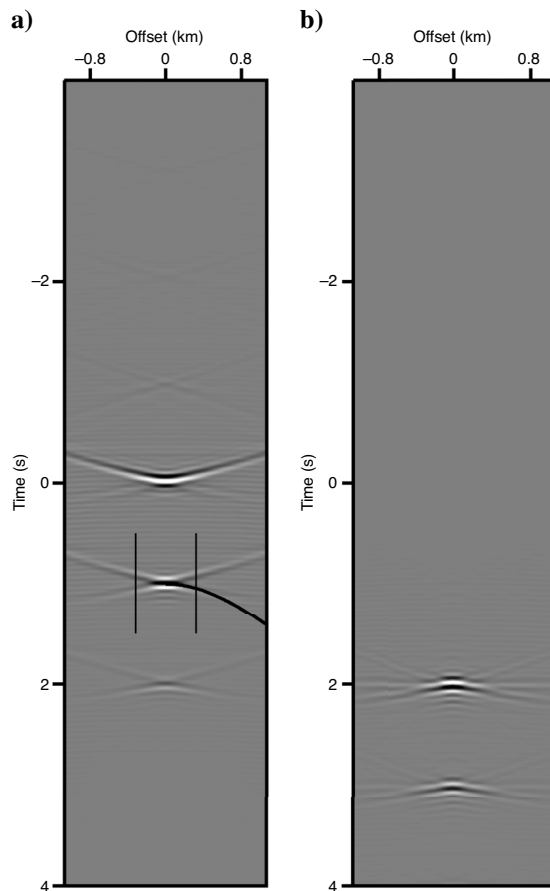

Figure 4. (a) Data downward continued to 1.5 km, the depth of the first reflector. The curve shows the expected moveout for the (primary) reflection from the bottom of the layer, and the vertical lines delineate the expected illumination of this reflection. (b) The estimated multiple, in the data, at a depth of 1.5 km; note the agreement with the true multiple in (a).
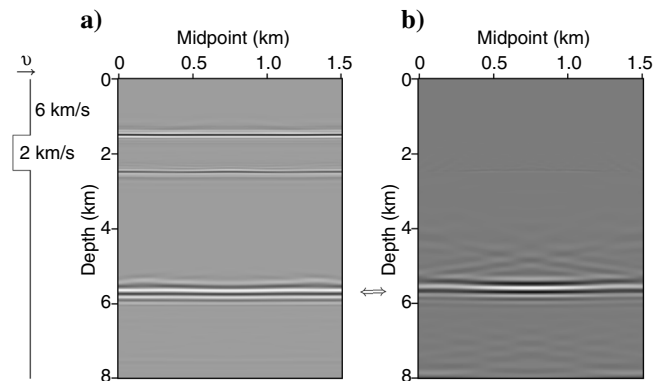

Figure 5. (a) The image with an artifact from a first-order internal multiple at about 5.7-km depth. (b) The estimated artifact.

tion from the bottom of the layer is at about $t = 1$ s, and the first-order internal multiple is at about $t = 2$ s.

We now estimate the multiples at depth by using equation 1. This estimation requires restricting $\tilde{d}$ to time $t > 0$. The procedure removes the primary reflection from the current depth (which theoretically arrives at $t = 0$), in this case 1.5 km, before doing the convolution. If this process is not done correctly and energy remains at $t \leq 0$, all primary reflections from deeper depths will be duplicated in the estimated-multiples section. In this model, a simple time-windowing procedure is sufficient because the reflections are far apart in time. Once the negative time contributions to the data have been removed, the data are convolved to estimate the multiple. The resulting wavefield is multiplied by an estimate of the image at the current depth (this is the $(E_1 a_1)(z, s', r')$ term appearing in equation 1) to give the estimate in Figure 4b. The event at about $t = 3$ s is a second-order internal multiple. This event is formed from the convolution of a primary with a first-order internal multiple. It is not present in the data panel because later arrivals were muted. These calculations complete step (b) in Figure 2.

We now proceed to (c) of the flowchart in Figure 2 and downward continue both the data and the estimated multiples to the next depth. From the data, an image at the current depth is formed containing both primaries and multiples, i.e., (d) in Figure 2. Another image is also computed at the current depth, containing an estimate of the artifacts caused by leading-order IM, i.e., (f) in Figure 2. The image containing both primaries and multiples gives the estimate $a_1(z, x)$ that feeds back into the estimation of the multiples through (e) of Figure 2.

Figure 5 compares the estimated artifact a_3 (Figure 5b) with the imaged data a_1 (Figure 5a). The estimated artifact overlays the artifact in the primary image.

Lens model

To illustrate the ability of the method to estimate multiples in more complicated velocity models, we add a low-velocity lens to the model. The resulting velocity model is shown in Figure 6. The lens is located in the center of the model; it is circular with Gaussian velocity variations, a diameter of 600 m, and a maximum contrast of −2 km/s. The addition of the lens has a large influence on the recorded data. The data from a midpoint of 9.8 km are shown in Figure 7. The first arrival is enlarged in Figure 7b to show the caustics caused by the lens more clearly. The estimated multiples in the image are shown in Figure 8. Once again, the multiple is relatively weak in the estimated image, because of the residual moveout on the common-image gathers, which are also shown in Figure 8. The image gathers were computed by using the method of Prucha et al. (1999).

To illustrate the dependence of this method on the background-velocity model, we now test the sensitivity of the estimated multiple artifact to errors in the velocity. In theory, knowledge of the velocity is necessary only to the depth of the shallowest reflection; in this case, the top of the layer at 2-km depth. To test this concept, we perturb the model by adding a second lens, with properties identical to the first lens, below the layer. The estimated artifact, shown in Figure 9, still matches the image artifact quite well. The tail on the far left of the image is likely the result of Fourier wrap-around in the propagator; other differences likely come from differences in illumination between estimated and true multiples.

To test the sensitivity of the method to errors in the velocity above the layer, we remove the lens and estimate the image and the multi-

ple in this incorrect velocity model. The results are shown in Figure 10. Although the estimated artifact remains at roughly the correct depth, the variation in the image with midpoint is not accurately estimated. Removing the lens entirely is a large change in the model; thus, we expect a large change in the image. In Figure 11, we demonstrate that we can still estimate the multiple with reasonable accuracy when the velocity perturbation is less dramatic. In this case, the lens has been moved 0.2 km shallower than in the true-velocity model, and the result is still acceptable.
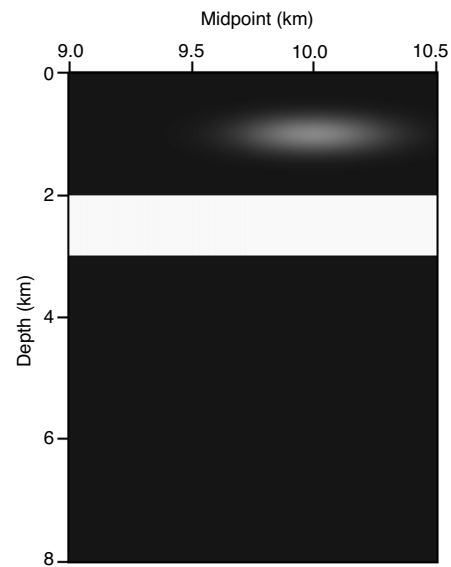

Figure 6. Velocity model, similar to the flat-layered example discussed previously, with the addition of a low-velocity lens to demonstrate that the method works in laterally heterogeneous velocity models.
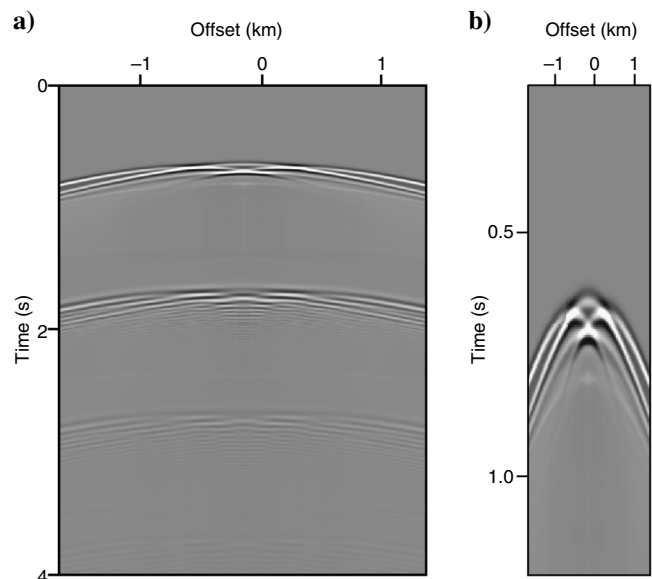

Figure 7. Common-midpoint gather at 9.8 km and zero depth, with only the offsets used to compute the images shown later. Note the triplications caused by the lens. (a) Full gather. (b) Zoom of the primary reflection from the top layer.
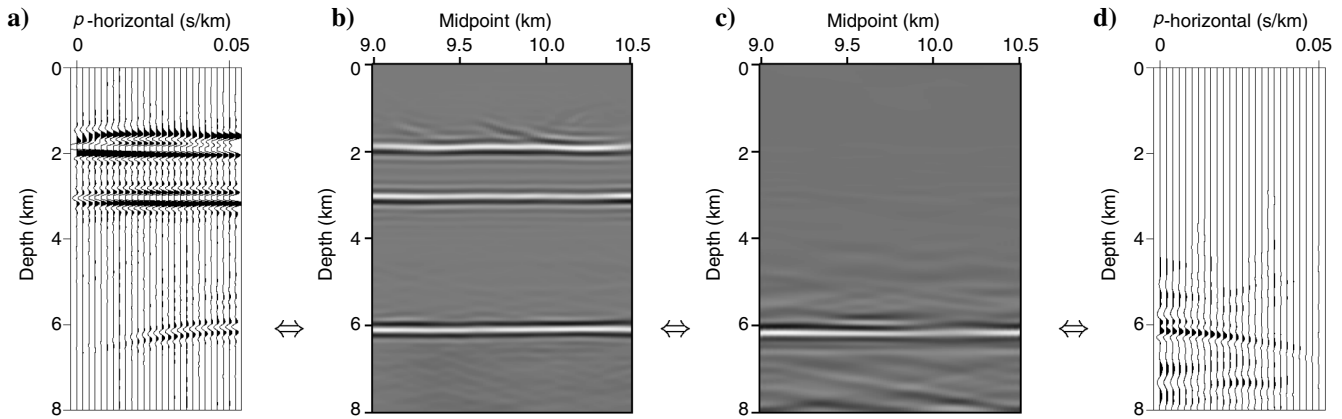
Figure 8. (a) Common-image gather for midpoint 9.8 km. (b) Image with an artifact from the first-order internal multiple at approximately 6 km depth. (c) Image of estimated artifacts from first-order internal multiples. (d) Image gather of estimated artifact. The label p-horizontal stands for the horizontal slowness.
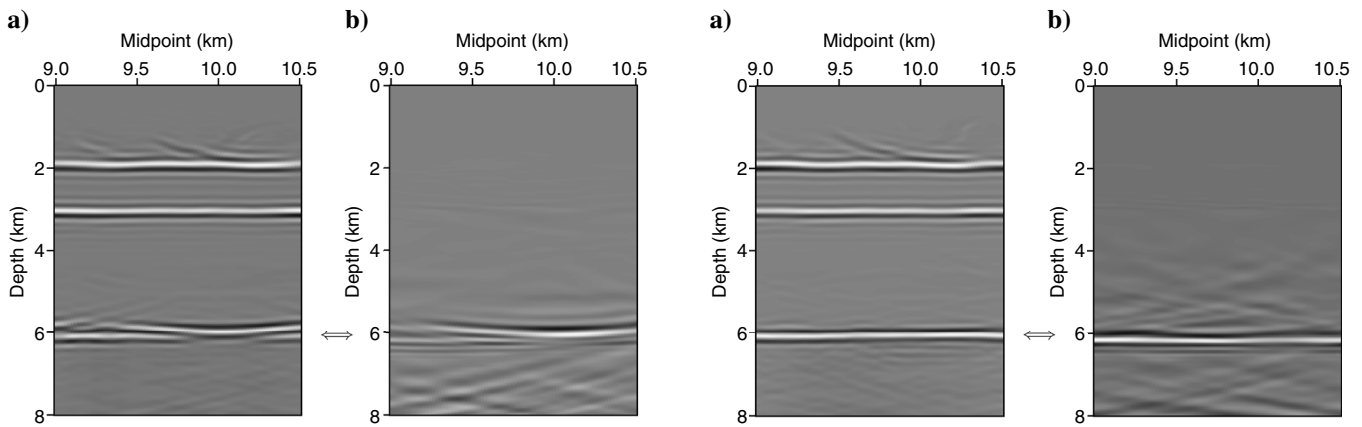

Figure 9. In these images, a second lens has been added beneath the layer to introduce a laterally varying velocity perturbation; this should not influence the accuracy of the estimated artifact. (a) Image with artifacts from internal multiples. (b) Estimated artifacts from first-order internal multiples.

Figure 11. In this model, the lens was moved 0.2 km deeper than in the correct velocity model. Because this perturbation is above the top of the layer, we expect an effect on the estimated multiple. (a) Image with artifacts from first-order internal multiples. (b) Estimated artifacts from first-order internal multiples.
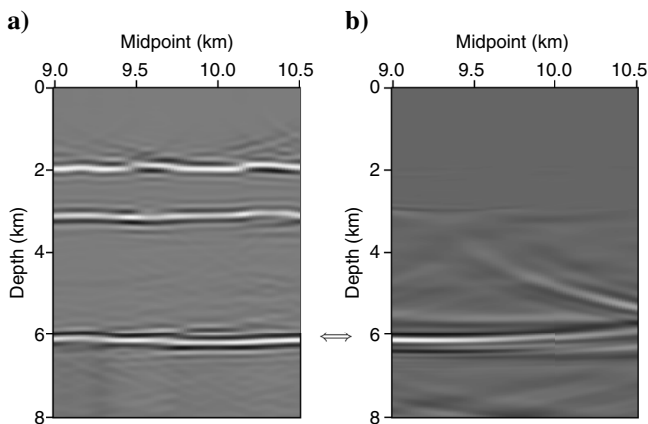

Figure 10. The lens was removed from the velocity model before generating these images. Because this perturbation is above the top of the layer, we expect this to have an impact on the estimated multiple. Note the change in the accuracy of the estimate beneath the lens. (a) Image with artifacts from first-order internal multiples. (b) Estimated artifacts from first-order internal multiples.

Field data

We present an example of the application of this method to field data. The data are from the Gulf of Mexico in a region with a large salt body. Estimating internal multiples in such an area is difficult because of multipathing introduced by the salt. The data have had standard preprocessing applied, including surface-related multiple elimination and a Radon demultiple; they have also been regularized to a uniform grid in the midpoint-offset coordinates. We show results from a single 2D line extracted from a 3D survey. Because the salt has a complicated 3D geometry, performing 2D imaging on this line is likely to introduce errors. Comparison with the image from a full 3D migration indicates that these effects are not overwhelming. Despite this, the estimated artifacts are likely to contain errors resulting from applying a 2D multiple-estimation algorithm in an area where the geology is 3D.

An image of the line is shown in Figure 12; the base of salt is indicated with the white arrows. The circled regions contain events, marked by black arrows, that are suspected to be artifacts caused by internal multiples. To compare the estimated artifacts with the arti-
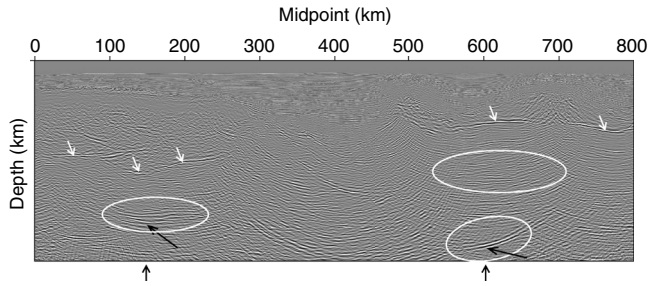
Midpoint (km)

Figure 12. Image for the field-data example. The base of salt is marked with white arrows, and the circles mark three areas of interest, two of which contain artifacts from internal multiples (left and top right) and one of which does not (bottom right). The locations of the CIGs shown in Figures 13 and 14 are marked with the black arrows below the image. The depth could not be displayed on this image; to tie the depth in Figure 13, the black arrow on the left image marks the artifact that arrow 4 points to in Figure 13 and the black arrow on the right of the image points to the position marked by arrow 3 in Figure 14.

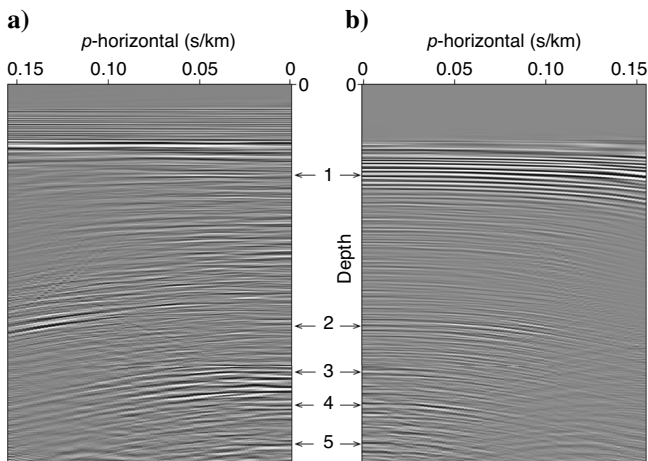**a)** *p*-horizontal (s/km)   **b)** *p*-horizontal (s/km)

Figure 13. Field-data example, common-image gather at CMP 150 (left black arrow in Figure 12). (a) The standard image gather. (b) The estimated artifacts from internal multiples. The five arrows indicate the locations of accurately estimated artifacts. Arrow 4 is the artifact marked with an arrow in the highlighted region on the image shown in Figure 12. The label *p*-horizontal stands for the horizontal slowness. The depth could not be displayed on these images.

facts seen in the image space, we show common-image gathers from two points in the model, marked by the black arrows beneath the image, covering the three highlighted areas.

The first image gather, shown in Figure 13, is approximately in the middle of the left highlighted region in Figure 12. There are five areas marked on this image gather at which artifacts are estimated and also occur in the imaged data. Arrow 4 marks the artifact in the left highlighted region of the image in Figure 12, indicating that this event is indeed an artifact caused by first-order internal multiples within the salt body. Arrow 1 marks a number of estimated artifacts mixed with primaries within and above the salt. It is possible that these artifacts are in fact residual energy from $t \leq 0$ that was incompletely removed. Arrow numbers 2, 3, and 5 indicate plausible internal multiples.

The second image gather, shown in Figure 14, is at CMP 600, in Figure 12 within the two highlighted regions on the right. First, note

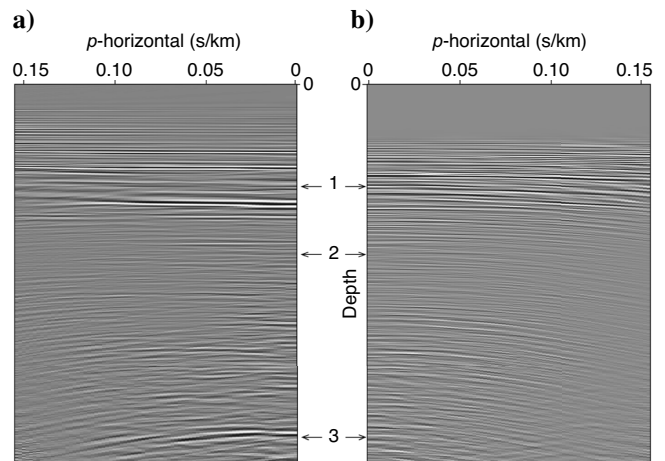**a)** *p*-horizontal (s/km)   **b)** *p*-horizontal (s/km)

Figure 14. Field-data example, common-image gather at CMP 600 (right black arrow in Figure 12). (a) The standard image gather. (b) The estimated artifacts from internal multiples. Arrows 1 and 2 indicate the locations of accurately estimated artifacts. Arrow 2 is within the upper-right highlighted region of the image. Arrow 3 marks the artifact in the lower-right highlighted region, marked with an arrow, on the image shown in Figure 12. That this artifact does not appear in the estimated artifacts indicates that this energy most likely does not come from an internal multiple. The label *p*-horizontal stands for the horizontal slowness. The depth could not be displayed on these images.

that arrow 3 indicates a strong event in the image gather that does not correspond to an estimated artifact. This is the event in the lower-right highlighted region of Figure 12 (marked by a black arrow). The absence of an estimated artifact at this position indicates that this energy is not an imaging artifact caused by internal multiples. It could be, for example, a primary that is migrated poorly resulting from inaccuracies in the velocity model, or residual energy from a surface-related multiple, or an out-of-plane effect. Arrows 1 and 2 mark other estimated artifacts in this image gather. Arrow 2 is in the second, shallower highlighted region of Figure 12, indicating that in this area, some of the energy does come from internal multiples.

In the common-image gathers, there are many estimated artifacts (Figure 14b) that are not easily correlated with events in the image gather made from the full data set (Figure 14a). Some of these estimated artifacts could have been attenuated by the Radon demultiple that has been applied to the data. Other sources of error include 3D effects, both in the image and in the estimation of the multiples, as well as amplitude errors in the estimated artifacts resulting in stronger amplitudes on the estimated artifacts than on the artifacts actually seen in the migration. This example is only intended to demonstrate the potential of the method.

CONCLUSION

We have described a method of estimating imaging artifacts caused by first-order internal multiples. This method requires knowledge of the velocity model down to the top of the layer that generates the multiple (the depth of the up-to-down reflection). The main computational cost of the algorithm comes from the downward continuation of the data and the internal multiples. Because two data sets are downward continued (the data themselves and the estimated multiples), the cost of the algorithm described here is about twice that of a usual prestack depth migration, plus the cost of the removal

of negative times. By estimating the multiples on downward-continued data, rather than in surface data, we avoid difficulties that may arise from caustics in the wavefield or the failure of the traveltime monotonicity assumption. In addition, estimating artifacts in the image rather than estimating multiples in the data shows clearly which part of the image has been contaminated by internal multiples, even if those multiples are poorly estimated or incompletely subtracted.

Although the method remains useful when multiples are poorly estimated or incompletely subtracted, reliable estimates of the amplitudes are important and remain a subject of future work. In addition, the dependence of this method on the velocity model could, in principle, be cast into a velocity-analysis procedure based on the move-out of multiples in the image gathers.

APPENDIX A

THE SCATTERING SERIES

The purpose of this and the following appendix is to give the theoretical background of the procedure described in the main text. This procedure has its roots in a hybrid series based on the Lippmann-Schwinger series, discussed in the seismic context by Weglein et al. (1997), and the generalized Bremmer series introduced by de Hoop (1996). The appendices highlight primarily how the Lippmann-Schwinger series enters our method; further details can be found in Malcolm and de Hoop (2005).

Constructing the hybrid series begins by decomposing the acoustic wavefield, u, into its up- and downgoing constituents $u_\pm$, as is done in the Bremmer series and in the development of the DSR equation (Claerbout, 1985). We first write the wave equation

$$c(z,x)^{-2}\partial_t^2 u - \partial_x^2 u - \partial_z^2 u = f, \qquad (A\text{-}1)$$

(in 3D, $x = (x_1, x_2)$) as a first-order system,

$$\partial_x \begin{pmatrix} u \\ \partial_z u \end{pmatrix} = \overbrace{\begin{pmatrix} 0 & 1 \\ c(z,x)^{-2}\partial_t^2 - \partial_x^2 & 0 \end{pmatrix}}^{A} \begin{pmatrix} u \\ \partial_z u \end{pmatrix} + \begin{pmatrix} 0 \\ -f \end{pmatrix},$$
$$(A\text{-}2)$$

where $c(z,x)$ is the isotropic velocity function and f is the source. In the Bremmer series, the wavefield is then split into its up- and downgoing constituents through

$$Q^{-1} = \begin{pmatrix} Q_+^* & Q_-^* \\ \mathcal{H}Q_+^{-1} & -\mathcal{H}Q_-^{-1} \end{pmatrix} \quad \text{and}$$

$$Q = \frac{1}{2}\begin{pmatrix} (Q_+^*)^{-1} & -\mathcal{H}Q_+ \\ (Q_-^*)^{-1} & \mathcal{H}Q_- \end{pmatrix}, \qquad (A\text{-}3)$$

where $\mathcal{H}$ denotes the Hilbert transform in time and * denotes adjoint. The component operators Q_- and Q_+ are pseudodifferential operators, which are a generalization of Fourier multipliers. In a constant-velocity medium, they simplify to a multiplication by $\left(\frac{\omega^2}{c^2} - \|k_x\|^2\right)^{1/4}$ in the Fourier domain. The form of the Q matrix in general, including the difference between the + and − operators, is discussed in Stolk and de Hoop (2005); for a short introduction to pseudodifferential operators, see de Hoop et al. (2003). The particular form used here is in the vertical acoustic-power-flux normalization. We choose this normalization because the transmission operators are of lower order than the reflection operators; see de Hoop (1996) for details on why this is the case and for other possible normalizations.

The Q matrix and its inverse complete the decomposition of the field into its up- and downgoing constituents, u_+ and u_-, so that

$$\begin{pmatrix} u \\ \partial_z u \end{pmatrix} = Q^{-1}\begin{pmatrix} u_+ \\ u_- \end{pmatrix}$$

and

$$\begin{pmatrix} f_+ \\ f_- \end{pmatrix} = Q\begin{pmatrix} 0 \\ f \end{pmatrix}. \qquad (A\text{-}4)$$

Applying the Q operators diagonalizes the system given in equation A-2, giving

$$\partial_z \begin{pmatrix} u_- \\ u_+ \end{pmatrix} = \begin{pmatrix} B_- & 0 \\ 0 & B_+ \end{pmatrix}\begin{pmatrix} u_- \\ u_+ \end{pmatrix} + \begin{pmatrix} f_- \\ f_+ \end{pmatrix}, \qquad (A\text{-}5)$$

where the subscript + indicates an upgoing quantity and the subscript − indicates downgoing; B is the single square-root operator.

We will denote by

$$L_0 = \begin{pmatrix} G_+ & 0 \\ 0 & G_- \end{pmatrix}, \qquad (A\text{-}6)$$

the matrix of one-way propagators (Green's functions) that solve the square-root equations for both up- and downgoing waves.

We have now set up the propagation of the wavefield through the square-root equation, but have yet to discuss the coupling of these components. It is here that we deviate from the formulation of the generalized Bremmer series. We couple the decomposed wavefield constituents to form a scattering series describing different orders of scattering using a contrast source formulation as in the Lippmann-Schwinger series (Weglein et al., 1997). This approach involves splitting the medium into a known background and an unknown contrast (difference between true and background) $\hat{V}$, which for the hybrid series is given by

$$\hat{V} = \frac{1}{2}\mathcal{H}\begin{pmatrix} Q_+ a Q_+^* & Q_+ a Q_-^* \\ -Q_- a Q_+^* & -Q_- a Q_-^* \end{pmatrix}, \qquad (A\text{-}7)$$

where $a = 2c_0^{-3}\delta c$ is the velocity contrast, c_0 denotes the (known) smooth background velocity, and δc denotes the nonsmooth velocity contrast. We use a subscript 0 to indicate the field in the background model and δ to represent a contrast; thus, the field U in the unknown true medium is related to that in the known background

medium by $U = U_0 + \delta U$. We denote by δU_j the matrix of up- and downgoing wave constituents scattered (transmitted or reflected) j times. From the Lippmann-Schwinger equation for the diagonalized system,

$$(I - \partial_t^2 \mathsf{L}_0 \hat{V}) \delta U = \partial_t^2 \mathsf{L}_0 \hat{V} U_0, \qquad (A\text{-}8)$$

we find that the terms in the hybrid forward-scattering series are related by

$$\delta U_1(\hat{V}) = - \partial_t^2 \mathsf{L}_0(\hat{V} U_0)$$

and

$$\delta U_m(\hat{V}) = - \partial_t^2 \mathsf{L}_0[\hat{V} \delta U_{m-1}(\hat{V})], \quad m = 2, 3, \ldots \; .$$
$$(A\text{-}9)$$

Equations A-9 describes the coupling of terms to form the scattered wavefield. Because L_0 and U_0 are in the diagonal system, the up- and downgoing wavefields are separated. The coupling operator $\hat{V}$ is a matrix that combines the up- and downgoing constituents of the wavefield to form the reflected or transmitted wavefield. The scattered field is the sum of these terms constituents

$$\delta U = \sum_{m \in \mathbb{N}} \delta U_j(\hat{V}). \qquad (A\text{-}10)$$

The operator L_0 introduced in equation A-6 solves the wave equation in the known background model. Equation A-10 is in the diagonal system and assumes that data can be collected at any point. We denote by R the restriction of the wavefield to the acquisition surface (depth $z = 0$), and define $\mathsf{M}_0 = R\mathsf{Q}^{-1}\mathsf{L}_0$; the Q^{-1} matrix maps back to the observable quantities. The data are then modeled as

$$\delta D = \begin{pmatrix} d \\ \partial_z d \end{pmatrix} = \partial_t^2 \mathsf{M}_0 \left\{ \hat{V} \left[U_0 + \sum_{m \in \mathbb{N}} (-1)^{m+1} \delta U_m(\hat{V}) \right] \right\}.$$
$$(A\text{-}11)$$

The first term on the right side of equation A-11 is the singly scattered data. The $m = 2$ term of the summation models triply scattered data, including first-order internal multiples. Malcolm and de Hoop (2005) show how an equation of the type given in equation 1 in the main text is derived from the third term of this series, meaning that internal multiples are third order in the contrast $\hat{V}$.

APPENDIX B

INVERSE SCATTERING

We have now constructed a forward series from which we can model data, given the contrast $\hat{V}$. In inverse scattering, the goal is to solve for $\hat{V}$ in terms of the data d. To this end, we rewrite equation A-8 as

$$- \partial_t^2 \mathsf{L}_0[\hat{V}(U_0 + \delta U)] = - \delta U, \qquad (B\text{-}1)$$

to motivate the expansion of $\hat{V}$

$$\hat{V} = \sum_{m \in \mathbb{N}} \hat{V}_m(d), \qquad (B\text{-}2)$$

where $\hat{V}_m$ is of order m in the data. Substituting this expression into equation A-11 leads to the following relationship between the $\hat{V}_m(d)$:

$$- \partial_t^2 \mathsf{M}_0(\hat{V}_m U_0) = - \partial_t^4 \mathsf{M}_0[\hat{V}_{m-1} \mathsf{L}_0(\hat{V}_1 U_0)], \quad m \geq 2, \quad (B\text{-}3)$$

along with the initiation of $\hat{V}_1$ in terms of the data $\delta D = \begin{pmatrix} d \\ \partial_z d \end{pmatrix}$:

$$\partial_t^2 \mathsf{M}_0(\hat{V}_1 U_0) = \delta D. \qquad (B\text{-}4)$$

Estimating $\hat{V}_1$ from equation B-4 is the standard seismic imaging problem. Stolk and de Hoop (2006) show that an image of the subsurface free of artifacts $\hat{V}$ is formed when a wave-equation migration is applied to the singly scattered data, $\partial_t^2 \mathsf{M}_0(\hat{V} U_0) = \delta D_1$. Applying such a migration to δD rather than to δD_1 gives $\hat{V}_1$, a first-order estimate of $\hat{V}$.

The recursion in equation B-3 shows that estimating higher-order contributions to the image (e.g., $\hat{V}_2$ or $\hat{V}_3$) does not require a separate imaging operator as each $\hat{V}_j$ can be estimated from $\hat{V}_{j-1}$; in fact, by continuing this argument, each term can be estimated from $\hat{V}_1$. For example, $\hat{V}_3$ is estimated from $\hat{V}_1$ by applying a migration operator to both sides of the expression

$$- \partial_t^2 \mathsf{M}_0(\hat{V}_3 U_0) = - \partial_t^6 \mathsf{M}_0\{\hat{V}_1 \mathsf{L}_0[\hat{V}_1 \mathsf{L}_0(\hat{V}_1 U_0)]\}. \quad (B\text{-}5)$$

The right side of equation B-5 is third order in $\hat{V}_1$, the linearized estimate of the contrast. In the previous section, we found that first-order internal multiples are third order in the true contrast $\hat{V}$. The right side of equation B-5 is an estimate (using $\hat{V}_1$ in place of $\hat{V}$) of the triply scattered data, of which first-order internal multiples form part. This result shows that multiples can be estimated from only $\hat{V}_1$, justifying the replacement of a with a_1 and the replacement of d_1 with d in equation 1.

Equation B-5, along with equation B-2, shows that a higher-order estimate of $\hat{V}$, namely, $\hat{V}_1 + \hat{V}_3$, is obtained by applying the standard wave-equation migration operator to an estimate of the multiples. In other words, two images are formed, one from all the data (a standard image) that will contain artifacts caused by multiples and another that estimates the subset of those artifacts that are caused by first-order internal multiples. The algorithm described in the main text comes from this observation.

REFERENCES

Aminzadeh, F., and J. M. Mendel, 1980, On the Bremmer series decomposition: Equivalence between two different approaches: Geophysical Prospecting, **28**, 71–84.
——, 1981, Filter design for suppression of surface multiples in a non-normal incidence seismogram: Geophysical Prospecting, **29**, 835–852.
Anstey, N. A., and P. Newman, 1966, The sectional auto-correlogram and the sectional retro-correlogram: Geophysical Prospecting, **14**, 389–426.
Artman, B., and K. Matson, 2007, Image-space surface-related multiple prediction: Geophysics, this issue.
Atkinson, F. V., 1960, Wave propagation and the Bremmer series: Journal of Mathematical Analysis and Applications, **1**, 225–276.
Berkhout, A. J., and D. J. Verschuur, 1997, Estimation of multiple scattering by iterative inversion, Part I: Theoretical considerations: Geophysics, **62**, 1586–1595.
——, 2005, Removal of internal multiples with the common-focus-point (CFP) approach: Part 1 — Explanation of the theory: Geophysics, **70**, no. 3, V45–V60.

Bremmer, H., 1951, The W. K. B. approximation as the first term of a geometric-optical series: Communications on Pure and Applied Mathematics, **4**, 105–115.

Claerbout, J. F., 1970, Coarse grid calculations of waves in inhomogeneous media with application to delineation of complicated seismic structure: Geophysics, **35**, 407–418.

——, 1985, Imaging the earth's interior: Blackwell Scientific Publications, Inc.

Corones, J. P., 1975, Bremmer series that correct parabolic approximations: Journal of Mathematical Analysis and Applications, **50**, 361–372.

de Hoop, M. V., 1996, Generalization of the Bremmer coupling series: Journal of Mathematical Physics, **37**, 3246–3282.

de Hoop, M. V., J. H. Le Rousseau, and B. Biondi, 2003, Symplectic structure of wave-equation imaging: A path-integral approach based on the double-square-root equation: Geophysical Journal International, **153**, 52–74.

Fokkema, J., R. G. Van Borselen, and P. Van den Berg, 1994, Removal of inhomogeneous internal multiples: 56th Annual Conference and Exhibition, EAGE, Extended Abstracts, Session H039.

Fokkema, J. T., and P. M. van den Berg, 1993, Seismic applications of acoustic reciprocity: Elsevier Science Publ. Co., Inc.

Gray, S. H., 1983, On the convergence of the time domain Bremmer series: Wave Motion, **5**, 249–255.

Jakubowicz, H., 1998, Wave equation prediction and removal of interbed multiples: 68th Annual International Meeting, SEG, Expanded Abstracts, 1527–1530.

Jin, S., R.-S. Wu, and C. Peng, 1998, Prestack depth migration using a hybrid pseudo-screen propagator: 68th Annual International Meeting, SEG, Expanded Abstracts, 1819–1822.

Kelamis, P., K. Erickson, R. Burnstad, R. Clark, and D. Verschuur, 2002, Data-driven internal multiple attenuation — Applications and issues on land data: 72nd Annual International Meeting, SEG, Expanded Abstracts, 2035–2038.

Kennett, B. L. N., 1974, Reflections, rays and reverberations: Bulletin of the Seismological Society of America, **64**, 1685–1696.

Lippmann, B. A., 1956, Rearrangement collisions: Physics Review, **102**, 264–268.

Malcolm, A. E., and M. V. de Hoop, 2005, A method for inverse scattering based on the generalized Bremmer coupling series: Inverse Problems, **21**, 1137–1167.

McMaken, H., 1986, On the convergence of the Bremmer series for the Helmholtz equation in 2D: Wave Motion, **8**, 277–283.

Moses, H. E., 1956, Calculation of scattering potential from reflection coefficients: Physics Review, **102**, 559–567.

Prosser, R. T., 1969, Formal solutions of inverse scattering problems: Journal of Mathematical Physics, **10**, 1819–1822.

Prucha, M. L., B. Biondi, and W. W. Symes, 1999, Angle common image gathers by wave equation migration: 69th Annual International Meeting, SEG, Expanded Abstracts, 824–827.

Razavy, M., 1975, Determination of the wave velocity in an inhomogeneous medium from reflection data: Journal of the Acoustical Society of America, **58**, 956–963.

Sava, P., and A. Guitton, 2005, Multiple attenuation in the image space: Geophysics, **70**, no. 1, V10–V20.

Sloat, J., 1948, Identification of echo reflections: Geophysics, **13**, 27–35.

Stolk, C. C., and M. V. de Hoop, 2005, Modeling of seismic data in the downward continuation approach: SIAM Journal of Applied Mathematics, **65**, 1388–1406.

——, 2006, Seismic inverse scattering in the downward continuation approach: Wave Motion, **43**, 579–598.

ten Kroode, A. P. E., 2002, Prediction of internal multiples: Wave Motion, **35**, 315–338.

van Borselen, R., 2002, Data-driven interbed multiple removal: Strategies and examples: 72nd Annual International Meeting, SEG, Expanded Abstracts, 2106–2109.

van Stralen, M. J. N., 1997, Directional decomposition of electromagnetic and acoustic wave-fields: Ph.D. thesis, Delft University of Technology.

Verschuur, D. J., and A. Berkhout, 1997, Estimation of multiple scattering by iterative inversion: Part II — Practical aspects and examples: Geophysics, **62**, 1596–1611.

——, 2005, Removal of internal multiples with the common-focus-point (CFP) approach: Part 2 — Application strategies and data examples: Geophysics, **70**, no. 3, V61–V72.

Weglein, A., F. B. Araújo, P. M. Carvalho, R. H. Stolt, K. H. Matson, R. T. Coates, D. Corrigan, D. J. Foster, S. A. Shaw, and H. Zhang, 2003, Inverse scattering series and seismic exploration: Inverse Problems, **19**, R27–R83.

Weglein, A., F. A. Gasparotto, P. M. Carvalho, and R. H. Stolt, 1997, An inverse-scattering series method for attenuating multiples in seismic reflection data: Geophysics, **62**, 1975–1989.